Title

More accurate trabecular bone imaging using UTE MRI at the resonance frequency of fat

Authors

Jerban, Saeed

Moazamian, Dina

Mohammadi, Hamidreza Shaterian

et al.

Publication Date

2024-07-01

DOI

10.1016/j.bone.2024.117096

Peer reviewed

Bone 184 (2024) 117096

Contents lists available at ScienceDirect

Bone

journal homepage: www.elsevier.com/locate/bone

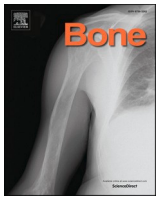

Full Length Article

More accurate trabecular bone imaging using UTE MRI at the resonance frequency of fat

Saeed Jerban [a,*,1], Dina Moazamian [a,1], Hamidreza Shaterian Mohammadi [a], Yajun Ma [a], Hyungseok Jang [a], Behnam Namiranian [a], Soo Hyun Shin [a], Salem Alenezi [b], Sameer B. Shah [c,d], Christine B. Chung [a,c], Eric Y. Chang [a,c], Jiang Du [a,c,*]

[a] Department of Radiology, University of California, San Diego, La Jolla, CA, USA
[b] Research and Laboratories Sector, Saudi Food and Drug Authority, Riyadh, Saudi Arabia
[c] Radiology Service, Veterans Affairs San Diego Healthcare System, San Diego, La Jolla, CA, USA
[d] Orthopaedic Research, University of California, San Diego, La Jolla, CA, USA

ARTICLE INFO

Keywords:
MRI
Fat peak frequency
Trabecular bone
UTE
Microstructure

ABSTRACT

High-resolution magnetic resonance imaging (HR-MRI) has been increasingly used to assess the trabecular bone structure. High susceptibility at the marrow/bone interface may significantly reduce the marrow's apparent transverse relaxation time (T2*), overestimating trabecular bone thickness. Ultrashort echo time MRI (UTE-MRI) can minimize the signal loss caused by susceptibility-induced T2* shortening. However, UTE-MRI is sensitive to chemical shift artifacts, which manifest as spatial blurring and ringing artifacts partially due to non-Cartesian sampling. In this study, we proposed UTE-MRI at the resonance frequency of fat to minimize marrow-related chemical shift artifacts and the overestimation of trabecular thickness. Cubes of trabecular bone from six donors (75 ± 4 years old) were scanned using a 3 T clinical scanner at the resonance frequencies of fat and water, respectively, using 3D UTE sequences with five TEs (0.032, 1.1, 2.2, 3.3, and 4.4 ms) and a clinical 3D gradient echo (GRE) sequence at 0.2 × 0.2 × 0.4 mm^3 voxel size. Trabecular bone thickness was measured in 30 regions of interest (ROIs) per sample. MRI results were compared with thicknesses obtained from micro-computed tomography (μCT) at 50 μm^3 voxel size. Linear regression models were used to calculate the coefficient of determination between MRI- and μCT-based trabecular thickness. All MRI-based trabecular thicknesses showed significant correlations with μCT measurements. The correlations were higher (examined with paired Student's *t*-test, $P < 0.01$) for 3D UTE images performed at the fat frequency ($R^2 = 0.59–0.74$, $P < 0.01$) than those at the water frequency ($R^2 = 0.18–0.52$, $P < 0.01$) and clinical GRE images ($R^2 = 0.39–0.47$, $P < 0.01$). Significantly reduced correlations were observed with longer TEs. This study highlighted the feasibility of UTE-MRI at the fat frequency for a more accurate assessment of trabecular bone thickness.

1. Introduction

Bone mineral density (BMD), as measured by dual-energy x-ray absorptiometry (DXA) at the spine or hip, is the standard clinical measure to diagnose osteoporosis and estimate bone fracture risk [1–4]. Despite the widespread use of BMD in clinics, a diagnosis of osteoporosis (based on DXA T-score ≤ -2.5) often fails to predict fracture risk accurately [5–12]. Notably, because of the DXA-based BMD two-dimensional (2D) nature, its measurement cannot detect local changes in bone structure.

High-resolution magnetic resonance imaging (HR-MRI) has been demonstrated as a promising tool for in vivo trabecular bone imaging [13–23]. MRI is a noninvasive three-dimensional (3D) imaging modality free from ionizing radiation, which is a significant advantage over standard 3D bone imaging modalities. For example, computed tomography (CT) may expose subjects to a considerable dosage of ionizing radiation, depending on the imaging coverage and resolution. HR peripheral quantitative CT (HR-pQCT) has a much lower radiation dose but is still a research modality used only in peripheral sites. Moreover, MRI can acquire structural and compositional information from surrounding soft tissues such as bone marrow [24,25], tendon [26],

* Corresponding authors at: Department of Radiology, University of California, San Diego, 9500 Gilman Dr., La Jolla, CA 92093, USA.
E-mail addresses: sjerban@health.ucsd.edu (S. Jerban), jiangdu@health.ucsd.edu (J. Du).
[1] Saeed Jerban and Dina Moazamian contributed equally to this research work.

https://doi.org/10.1016/j.bone.2024.117096
Received 6 December 2023; Received in revised form 18 March 2024; Accepted 8 April 2024
Available online 15 April 2024

cartilage [27], and muscle during the same scan session for more thorough pathological assessments.

HR MRI indirectly visualizes trabecular bone as dark regions surrounded by marrow with bright signals, because trabecular bone has much lower proton density and shorter apparent transverse relaxation time (T2*) than marrow[28]. Such indirect visualization has been used to track changes in trabecular bone microstructure in response to medical treatments [29–31] and for finite element analysis (FEA) based assessment [23,32]. With image post-processing, it is possible to render the 3D architecture and extract the corresponding structural parameters of trabecular bone [28,33–36]. Considering the average size of trabecular bone, the in-plane HR MRI pixel sizes are often selected to be near 0.2 mm [23,37].

The susceptibility difference between trabecular bone and bone marrow [38,39], the heterogeneity of complex hierarchical bone structure [40], and the presence of multiple fat resonance peaks [39], all contribute to the reduction in marrow T2*, resulting in marrow signal loss and thus an overestimation of trabecular bone thickness. Specifically, a portion of marrow at the bone boundary (reduced T2*) is likely to be considered as bone, falsely, by image thresholding and segmentation methods. Ultrashort echo time MRI (UTE-MRI) allows for acquiring signals from tissues with short T2* [41,42], such as bone and its neighboring marrow. UTE-MRI can minimize signal loss due to T2* shortening. Furthermore, the non-Cartesian sampling techniques such as radial or rosette/petal trajectories employed in UTE-MRI offer distinct advantages over Cartesian sampling employed in conventional MRI, providing improved k-space coverage and reduced susceptibility to motion artifacts, which is particularly beneficial for applications requiring motion robustness [43]. However, UTE-MRI is sensitive to chemical shift artifacts, which manifest as spatial blurring and ringing artifacts due to non-Cartesian sampling [44]. Specifically, in Cartesian sampling, the chemical shift artifact occurs in the frequency-encoding direction as a shift in the spatial location of fat voxels (no chemical shift artifact in the phase encoding direction). In non-Cartesian 3D UTE sampling, the frequency encoding is performed in three dimensions. As a result, spatial misregistration and ringing artifacts happen in all directions.

In this study, we proposed UTE-MRI at the resonance frequency of fat to minimize marrow-related chemical shift artifacts and signal loss due to susceptibility-induced T2* shortening, thereby reducing the overestimation of trabecular thickness. It is hypothesized that HR UTE-MRI can minimize marrow-related chemical shift artifacts if the center frequency is shifted to the fat peak. Bone is expected to be off-resonance in fat-centered imaging. However, bone signal, while detectable with UTE-MRI, is much lower than marrow signal due to its low proton density and ultrashort T2*. As a result, a negligible water-associated off-resonance artifact is anticipated. We will investigate the feasibility of HR UTE-MRI at the fat peak frequency for a more accurate depiction of trabecular bone structure in human distal tibial specimens at 3 T. MRI-based trabecular bone thickness, the most common measure used in the literature, will be compared with the micro-computed tomography (μCT) results [21,45–53].

2. Materials and methods

2.1. Sample preparation

Fresh-frozen cadaveric specimens of the tibia from six donors (75 ± 4 years old) were provided by the UC San Diego School of Medicine Medical Education/Anatomical Services. The axial section of the distal tibia, 30 to 50 mm above the medial malleolus, was cut into ~20 mm segments using a commercial band saw. One 20 mm^3 cube was excised from the bone metaphysis region of each specimen using a low-speed diamond saw (Isomet 1000, Buehler, IL). Only trabecular bone was included in the final bone cubes. After being thawed, trabecular bone cubes were soaked in perfluoropolyether (Fomblin, Ausimont, Thorofare, NJ) and placed under a negative pressure vacuum for about 2 h to reduce air bubbles. Next, specimens were placed in a rectangular plastic container (80 × 100 × 40 mm, approximately) filled with perfluoropolyether to minimize dehydration and susceptibility artifacts during the MRI scans.

2.2. UTE-MRI protocol

The UTE-MRI scans were performed on a 3 T clinical scanner (GE Healthcare, Waukesha, WI) using an eight-channel transmit and receive knee coil. A 3D UTE Cones sequence with TR = 12.1 ms and five TEs (0.032, 1.1, 2.2, 3.3, and 4.4 ms) and a clinical 3D Cartesian gradient echo (GRE) sequence (TR = 9.6 ms, TE = 4.4 ms) were performed twice, first at the water peak frequency and then at the fat peak frequency. The fat peak frequency was selected by the MR operator after performing a manual pre-scan. The field-of-view (FOV), acquisition matrix, slice thickness, voxel size, and number of slices were 80 mm, 400 × 400, 0.4 mm, 0.2 × 0.2 × 0.4 mm^3, and 160. The approximate scan time was 8.5 min for 3D UTE and 12.8 min for GRE sequences, respectively.

2.3. Micro-computed tomography (μCT)

Specimens were also scanned using a GE eXplore 120 Preclinical μCT scanner at 50 μm^3 isotropic voxel size. Other scanning parameters were as follows: FOV = 100 mm, 60 kV voltage, 32 mA current, 0.5° rotation step, number of averages per frame = 2, and 80 min total scan time.

2.4. MRI and μCT image analysis

MRI images were analyzed using 10 slices in the middle of each specimen, covering 4 mm in the Z direction. Three ROIs were selected at each slice by an experienced image analyst while avoiding regions affected by infiltrated air bubbles. 30 ROIs per specimen (180 ROIs for six specimens) were selected in total. Corresponding μCT images were selected manually (8 consecutive μCT slices for each MRI slice). A 2D semiautomatic registration algorithm was used to map the selected ROIs onto the μCT images. Registration was performed after selecting the matching corners of each specimen in MRI (moving in the registration) and μCT (fixed in the registration) images. Notably, employing a 3D automatic registration algorithm was not applicable due to the artifacts in MRI images caused by the trapped air in the marrow space. Also, selecting ROIs on registered MR images would make it difficult to detect and avoid air bubbles, as enlarged registered MR images looked noisier and did not cover the entire specimen.

A local adaptive gray level thresholding algorithm was used to segment bone pixels from marrow pixels within each selected polygon ROI with a size of ~1.5 × 1.5 cm^2 on the MRI and μCT images. Local thickness was calculated at each pixel using the distance transform performed on the segmented images. Specifically, the local trabecular thickness in a 2D fashion equals the diameter of the largest covering circle (Fig. 3H).

For each ROI in MRI images, the contrast-to-noise ratio (CNR) was calculated between the bone and marrow regions ($CNR = (Signal_{marrow} - Signal_{bone})/Noise_{background}$). CNR is expected to always be a positive variable as marrow demonstrates a higher signal than bone.

2.5. Statistical analysis

A simple linear regression model of MRI-based trabecular bone thickness as a function of μCT-based trabecular bone thickness was defined ($MRI_{Th} = A \times \mu CT_{Th} + B$, where A and B are constant values) to calculate the coefficient of determination, R^2. The statistical significance was determined using the Student's *t*-test. To ensure that intra-specimen dependency did not affect the results, all correlation studies were repeated using one average measure per sample instead of multiple

ROIs. All image processing steps and statistical analyses were performed using in-house developed programs in MATLAB (version 2021, The Mathworks Inc., Natick, MA, USA). *P* values <0.05 are considered as significant.

3. Results

Fig. 1 shows HR MR images of a representative distal tibia specimen acquired at the fat peak frequency and water peak frequency, respectively, using 3D UTE acquisition with a TE of 0.03 ms. Significant chemical shift artifacts were observed in UTE images acquired at the water peak frequency (arrows in Fig. 1A), blurring trabecular bone structure (Fig. 1A and zoomed Fig. 1C). In contrast, UTE images acquired at the fat peak frequency showed no noticeable chemical shift artifacts (Fig. 1B and zoomed Fig. 1D), providing a superior depiction of trabecular bone structure. The contrast between bone and marrow is noticeably higher in UTE images acquired at the fat peak frequency than at the water peak frequency.

Fig. 2 shows HR MR images of the same distal tibia specimen (Fig. 1) acquired at the fat peak frequency using 3D UTE acquisition with increasing TEs from 0.03 ms to 4.4 ms (Fig. 2A–E and zoomed Fig. 2G–K). These images are visually compared with 3D GRE (Fig. 2F and zoomed Fig. 2J) acquisition at the fat peak frequency. The darker pixels within the specimens represent the trabecular bone, which seems larger and overestimated with increasing TEs (from the left column to the right column subfigures). Interestingly, the darker regions seem more pronounced at TE 1.1 ms and 3.3 ms in some locations (indicated with thin arrows and arrowheads in the lower row) due to the water and fat out-phase spins canceling their net transverse magnetization at the marrow/bone boundaries.

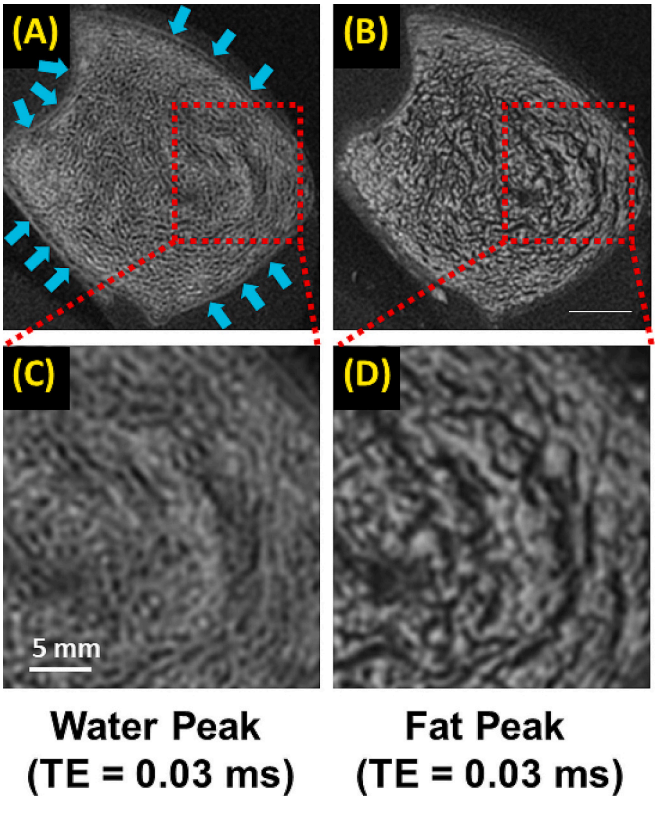

Fig. 1. A representative trabecular bone specimen from the distal tibial was imaged in the axial plane using the 3D UTE sequence at the water peak frequency (A) and the fat peak frequency at TE = 0.03 ms (B). The corresponding zoomed regions indicated with the red dashed-line boxes are shown in the second row (C–D). The voxel size in all images is 0.2 × 0.2 × 0.4 mm^3. UTE images acquired at the water peak frequency show significant chemical shift artifacts, manifesting as blurred trabecular bone structure and ringing artifacts compared to the fat peak. The contrast between bone and marrow is noticeably higher in UTE images acquired at the fat peak frequency than at the water peak frequency.

Fig. 3 shows a representative trabecular bone section used for MRI- and μCT-based assessment of the trabecular bone thickness. UTE-MRI at the fat peak frequency shows excellent bone marrow structure in the axial plane at 0.2 × 0.2 × 0.4 mm^3 voxel size (Fig. 3A, D). Trabecular bone shows as signal void due to its much lower proton density and shorter T2* relaxation time. Simple signal inversion reversed the image contrast with a high signal from trabecular bone and a low signal from marrow (Fig. 3B, E). Fig. 3C and F shows the corresponding μCT images acquired at 0.05 × 0.05 × 0.05 mm^3 voxel size. Fig. 3G shows the schematics of the trabecular bone boundaries in a small zoomed-in section. The schematic largest covering circles used to calculate the local bone thickness are depicted in Fig. 3H.

Fig. 4 shows the local trabecular thickness map within a representative ROI selected manually (at the fat peak frequency UTE image) to avoid artifacts caused by air trapped in the bone of the same representative trabecular bone section in Fig. 3. The local trabecular thicknesses were calculated based on the MR images at the fat peak frequency (3D UTE at TEs = 0.03, 1.1, 2.2, 3.3, and 4.4 ms and GRE at TE = 4.4 ms), and based on the ground truth μCT images, respectively. The estimated local trabecular thickness was higher for MR images acquired at longer TEs. MRI-based trabecular thicknesses were noticeably higher than μCT-based results.

Fig. 1S in the Supplemental materials demonstrates the local trabecular thickness maps using the corresponding MR images centered on the water peak frequency.

Fig. 5 demonstrates the scatter plots and the linear regressions of the MRI-based trabecular thicknesses on the μCT-based results, including 30 ROIs per specimen (180 ROIs for six specimens, degrees of freedom = 178). All MRI-based trabecular thicknesses showed significant correlations with the μCT-based results. The correlations were higher for 3D UTE MR images performed at the fat peak frequency (R^2 = 0.59–0.74, $P < 0.01$, F-value =198–502) than those at the water peak frequency (R^2 = 0.18–0.52, $P < 0.01$, F-value = 40–189). UTE and TE =1.1 ms images at the fat peak frequency had higher correlations (R^2 = 0.74 and 0.73, F-value =502 and 494, respectively, $P < 0.01$) with μCT-based results than UTE images acquired at longer TEs (R^2 = 0.59–0.67, $P < 0.01$, F-value =198–358), or UTE images acquired at the water peak (R^2 = 0.18–0.52, $P < 0.01$, F-value = 40–189), or the clinical GRE images (R^2 = 0.47 and 0.53, $P < 0.01$, F-value = 158 and198).

Fig. 6 demonstrates similar scatter plots and the linear regressions when the bone thicknesses were averaged per specimen ($n = 6$, degrees of freedom = 4) to ensure that intra-specimen dependency does not affect the results. All trabecular thicknesses from fat peak frequency MRI showed significant correlations with the μCT-based results (R^2 = 0.88–0.99, $P \leq 0.01$, F-value =20–264). For trabecular bone thicknesses from water peak frequency MRI, correlations were statistically significant only for images at TE = 1.1 (R^2 = 0.81, $P = 0.01$, F-value =17) and TE = 4.4 ms (R^2 = 0.78 and 0.82, $P = 0.02$ and 0.01, F-value =14 and 18, respectively). UTE and TE = 1.1 ms images at the fat peak frequency had the highest correlations with μCT-based results (R^2 = 0.95 and 0.99, F-value =73 and 264, respectively, $P < 0.01$). In summary, using the paired Student's *t*-test, the MRI-μCT correlations were significantly higher ($P < 0.01$) when 3D UTE MR images were performed at the fat peak frequency than those at the water peak frequency.

Fig. 2S in the Supplemental materials demonstrates the average CNR between the trabecular bone and the marrow in the studied specimens using different 3D UTE MRI sequences. Fat-centered 3D UTE images showed higher CNRs than water-centered images. The UTE image at the fat peak frequency showed the highest CNR compared with other acquisitions.

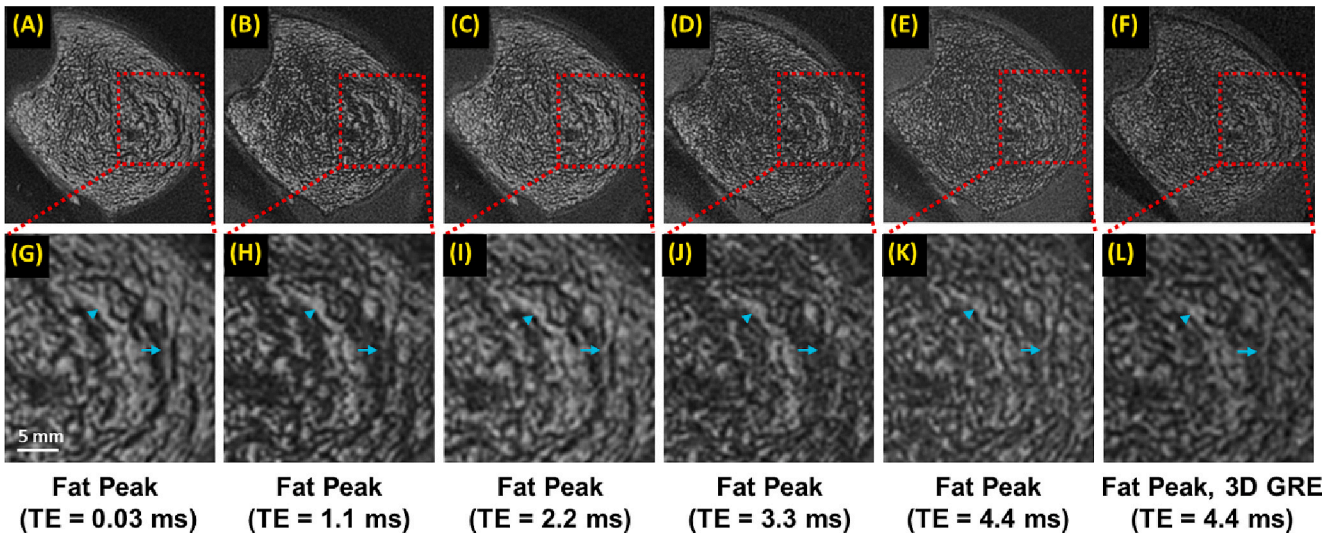

Fig. 2. A representative trabecular bone specimen from distal tibial imaged in the axial plane using 3D UTE sequence at the fat peak frequency at TE = 0.03 ms (A), TE = 1.1 ms (B), TE = 2.2 ms (C), TE = 3.3 ms (D), and TE = 4.4 ms (E), and clinical GRE (3D-Cartesian) sequence at TE = 4.4 ms (F). The corresponding zoomed regions indicated with the red dashed-line boxes are shown in the second row (G-L). The voxel size in all images is 0.2 × 0.2 × 0.4 mm^3. The darker region associated with the trabecular bone increased with TE, leading to an overestimation of trabecular thickness.

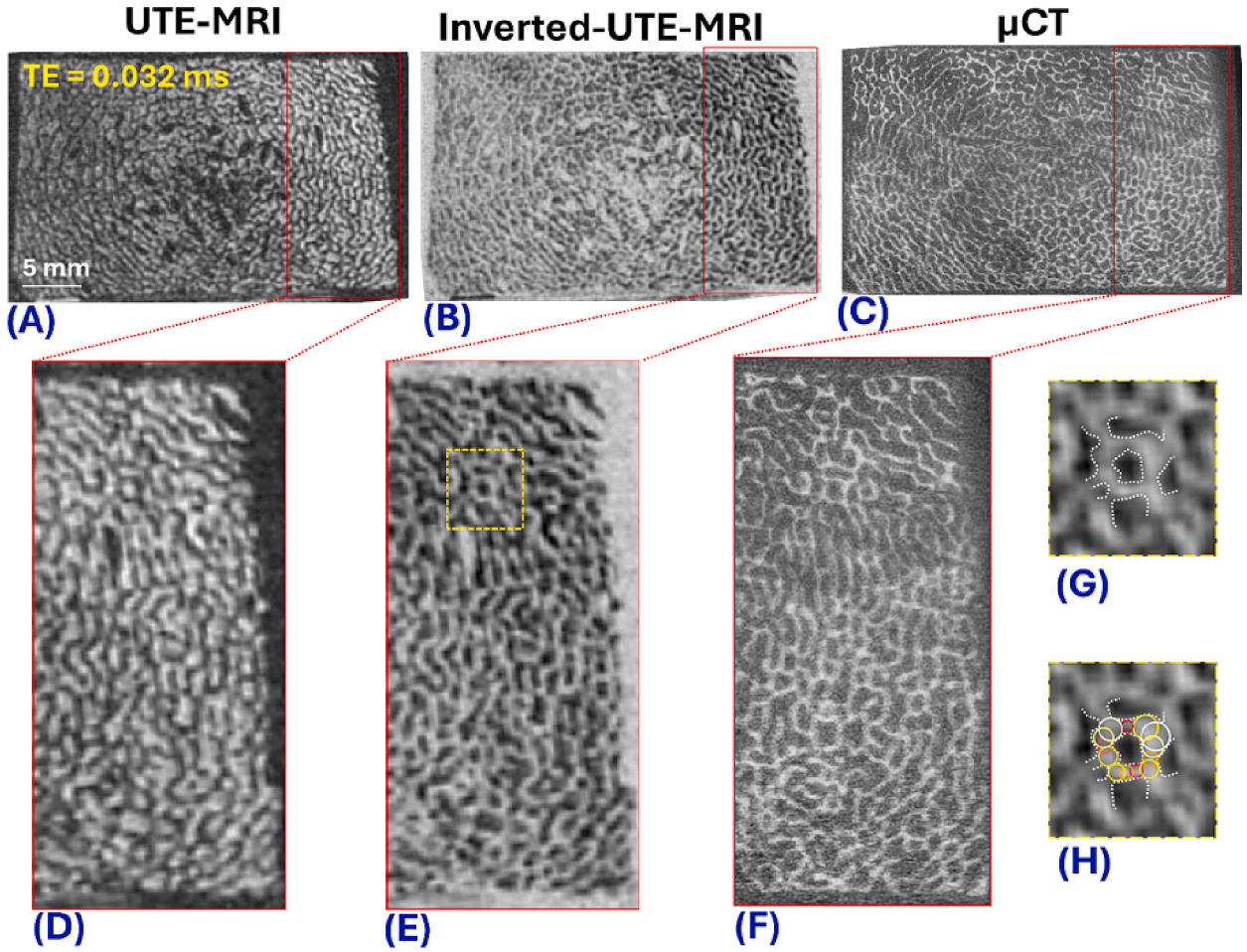

Fig. 3. A representative trabecular bone specimen (excised cube from metaphysis in distal tibial) in the axial plane using 3D UTE sequence (0.2 × 0.2 × 0.4 mm^3 voxel size) acquired at the fat peak frequency, TE = 0.032 ms (A). Signal inversion of 3D UTE image highlights trabecular bone structure (B). μCT provides high isotropic (0.05 × 0.05 × 0.05 mm^3 voxel size) imaging of trabeculae (C). The corresponding zoomed regions indicated with the red boxes are shown in the second row (D–F). Schematics of the trabecular bone boundaries (G) and the largest covering circles to calculate the local bone thickness (H). The thin regions of bone are indicated with small covering circles in red, while the thick regions are indicated with larger covering circles in yellow and white.

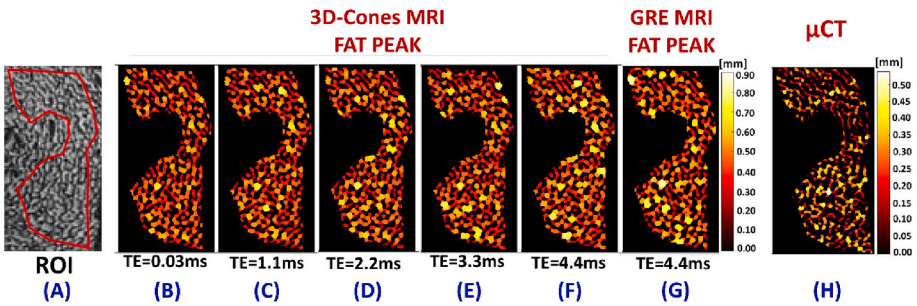

Fig. 4. A representative ROI selected on the fat peak frequency UTE image (A), and the corresponding local trabecular bone thickness map generated for TE = 0.03 ms (B), TE = 1.1 ms (C), TE = 2.2 ms (D), TE = 3.3 ms (E), and TE = 4.4 ms (F). The trabecular thickness maps for the matched representative ROI on the clinical GRE (G) and μCT images (H) are also shown. The estimated local trabecular thickness was higher for MR images acquired at higher TEs. MRI-based trabecular thicknesses were obviously higher than μCT-based results.

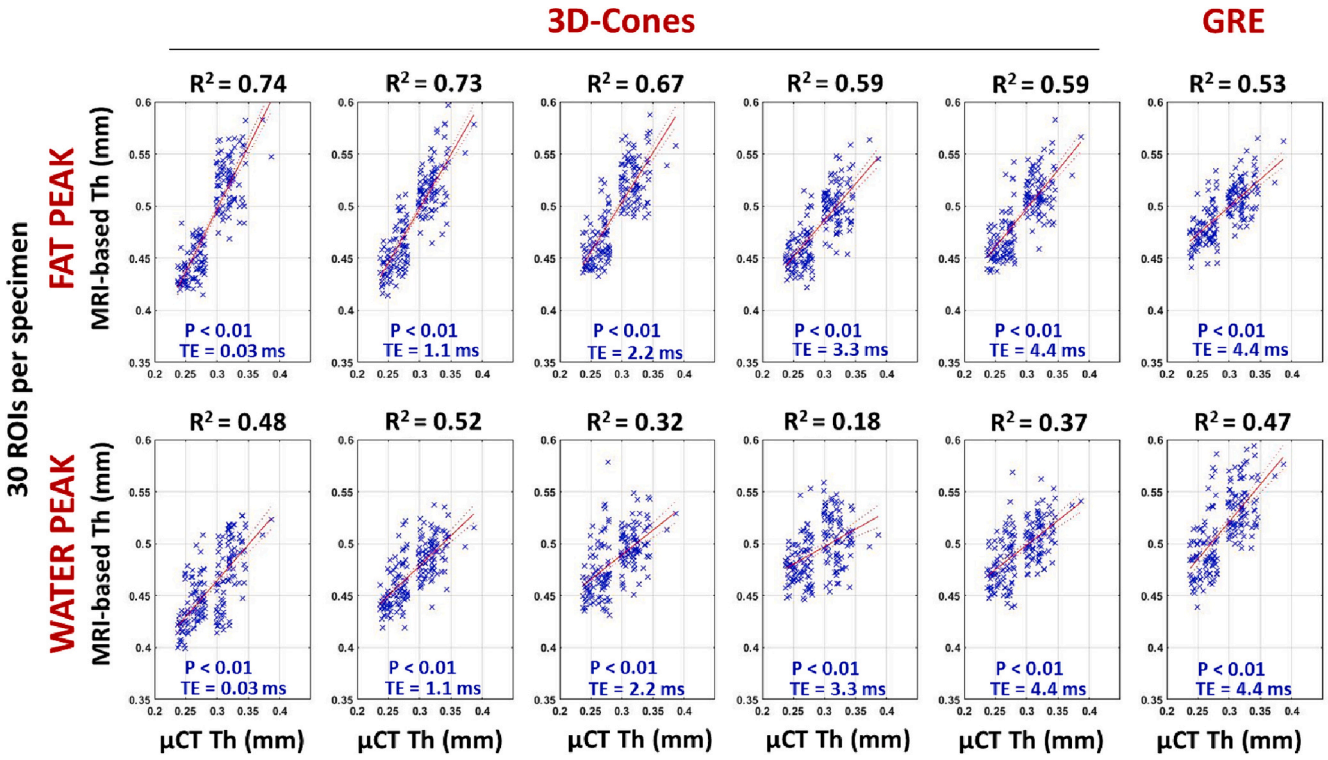

Fig. 5. Scatterplots and linear regressions of MRI-based trabecular bone thicknesses on the μCT-based results, including 30 ROIs per specimen (n = 180).

4. Discussion

This study was the first to investigate the feasibility of using UTE-MRI at the fat peak frequency to improve trabecular bone thickness assessment. The μCT-based trabecular bone thickness strongly correlated with MRI-based results when the fat peak frequency UTE or TE = 1.1 ms images were used. Correlations were lower on average when higher TEs were utilized. The μCT-MRI correlations were higher for MR images performed at the fat peak frequency than those at the water peak frequency, on average. UTE MR imaging centered on the fat peak frequency significantly minimized marrow-related chemical shift artifacts. Specifically, bone trabeculae are expected to be off-resonance in fat-centered imaging, and due to the much lower signal in bone than in marrow, the water-associated off-resonance artifact is negligible. Meanwhile, UTE data acquisition minimizes signal loss due to susceptibility-induced T2* shortening. As a result, UTE MRI at the fat peak frequency improves indirect imaging of trabecular bone by resolving chemical shift artifacts while minimizing susceptibility effects. The superior performance of fat-centered UTE-MRI is likely to be more pronounced when a higher fat fraction in the marrow is expected, such as in older osteoporotic patients, particularly in their lower extremities [54–56]. Nevertheless, such hypotheses are to be examined in future investigations.

Trabecular bone thickness has been the most used metric in the literature for trabecular evaluation [21,45–53]. Thus, an accurate MRI-based trabecular thickness is of great interest to the bone research community. Moreover, accurate rendering of trabecular bone structure can be coupled with micro-FEA to assess bone mechanical competence [23]. Predicting the mechanical properties of bone, particularly in trabecular bone sites, is challenging because of bone's heterogeneous and anisotropic nature, such as the dependencies on loading direction, anatomical location, and sample dimension [57–59]. In micro-FEA, the displacements, forces, and stress and strain tensors can be calculated throughout the meshed volume of trabecular bone to predict its mechanical competence. Developing micro-FEA based on fat-centered UTE imaging of trabecular bone is likely to improve mechanical competence prediction, which has not been investigated yet [23].

In addition to HR structural MRI, other MRI-based techniques for

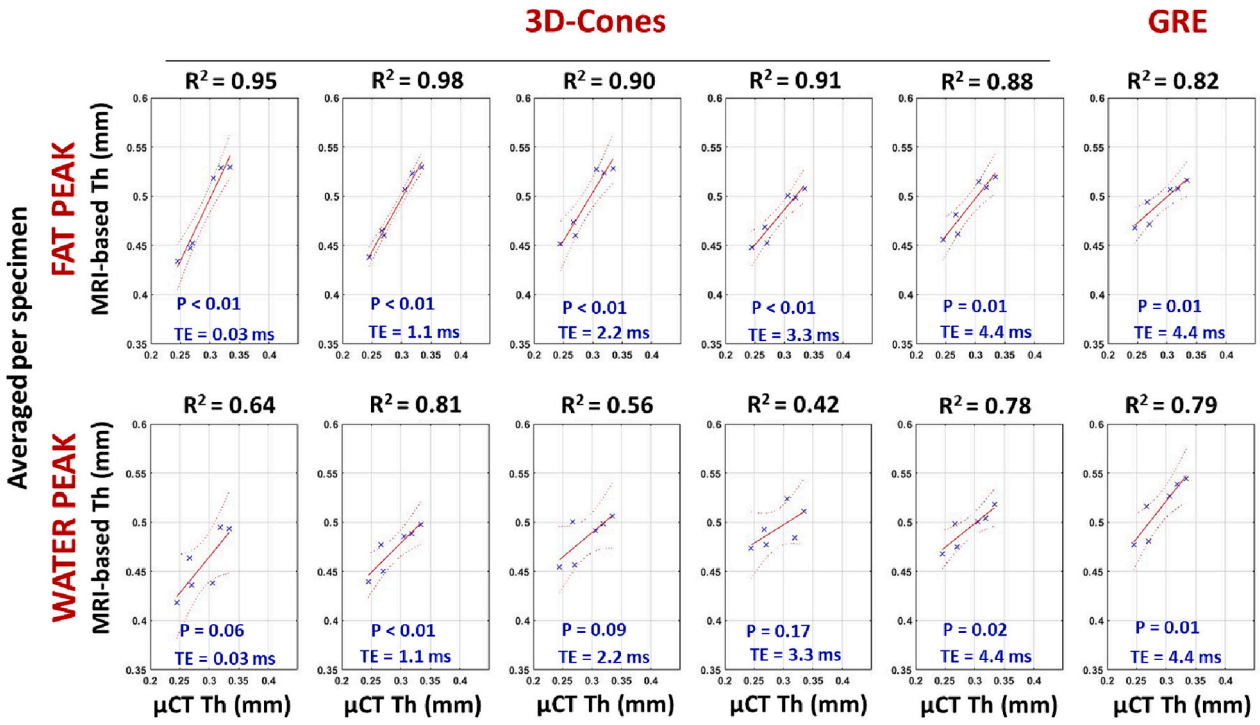

Fig. 6. Scatterplots and linear regressions of MRI-based trabecular bone thicknesses on the μCT-based thickness. All thicknesses were averaged per specimen ($n = 6$).

trabecular bone assessment can be categorized into two groups: bone-marrow relaxometry (T1, T2*, and T2′ analyses) in relatively low-resolution images [33,60–65], and direct bone imaging via UTE-MRI with marrow signal suppression [66–69]. Most low-resolution MRI-based analyses of trabecular bone have been focused on marrow relaxometry or magnetic susceptibility measurements [33,60–65]. These techniques can indirectly quantify trabecular bone density and structure [41,53,54,63]. The strong susceptibility between trabeculae and marrow interface leads to greatly reduced relaxation times for bone marrow, depending on bone volume and bone-specific surface [33,62]. Bone marrow relaxation times are correlated with BMD in different studies [28,33,48,62,63,70], however as determined by the low image resolution, they are not capable of trabecular bone thickness assessment achievable by the proposed fat-centered UTE MRI technique. Direct trabecular bone imaging has been reported using water- and fat-suppressed MRI techniques [66–69]. To selectively image trabecular bone, it is critical to suppress signals from long T2 tissues, particularly marrow fat, because of its much higher signal than bone. The fat-suppressed UTE sequence detects signals from water bound to the organic matrix [71], thereby providing an indirect measurement of organic matrix density in trabecular bone [69]. However, this technique is subject to an inherently low signal-to-noise ratio (SNR) efficiency due to the low water concentration in porous trabecular bone. It is difficult or impossible to directly image the trabecular bone networks, therefore fat-suppressed UTE sequences are able to map organic matrix density but unable to assess the trabecular bone thickness, which is achievable with the fat-centered UTE-MRI technique.

The limitations of this study can be described in the following five aspects. First, this study was performed on bone specimens cut from the bone metaphysis region, in which cortical bone and the surrounding muscles were removed. The presence of muscles, other soft tissues, and subject motion will contribute to the reduced performance of all HR MR imaging techniques in vivo compared with ex vivo studies. However, it is possible to apply the fat-centered UTE-MRI technique to assess trabecular bone structure in vivo, as demonstrated in the Supplemental Fig. 3S. The calcaneal trabecular bone of a 43-year-old male volunteer was depicted with higher contrast in images acquired at the fat peak frequency than the water peak frequency and greater marrow signal loss was observed in images acquired at longer TEs. Future in vivo investigations are necessary to demonstrate the superiority of fat-centered UTE imaging for better depiction of trabecular bone microstructure. Second, FEA based on MRI data would provide interesting comparisons between the examined sequences. In future studies, the FEA of trabecular bone structure based on fat-centered UTE-MRI is expected to provide more accurate bone mechanical characteristics. Third, the HR MR imaging was performed using an anisotropic voxel size, which was appropriate based on the authors' experience. Future investigations should be performed to seek the practical anisotropic and isotropic voxel sizes for optimal human trabecular bone depiction with sufficient signal-to-noise ratio while avoiding long scan times. Fourth, the trabecular number is an important outcome but was not investigated. Fourth, Fourth, the trabecular number is an important outcome but was not investigated. This study only focused on the trabecular bone thickness. The performance of the proposed UTE-MRI sequence in detecting the number of trabeculae should be investigated in future studies. Fifth, this study was performed using UTE sequences. While all the major MR vendors have UTE techniques or variants available on their systems, these sequences are still in the research stage, which limits their availability to other researchers and clinicians.

5. Conclusions

The feasibility of UTE-MRI at the fat peak frequency for more accurate trabecular bone assessment was investigated for the first time in the literature. The correlations between μCT- and MRI-based trabecular thicknesses were higher when MR was performed at the fat peak frequency instead of the water peak frequency. UTE MRI at the fat peak frequency minimizes the marrow-related chemical shift artifacts and susceptibility-induced T2* shortening simultaneously. The μCT-based trabecular bone thickness strongly correlated with MRI-based results when the fat peak frequency UTE or TE = 1.1 ms images were used. Correlations were lower on average when higher TEs were utilized. This study highlighted the feasibility of UTE at the fat peak frequency for a more accurate trabecular bone thickness assessment.

CRediT authorship contribution statement

Saeed Jerban: Writing – review & editing, Writing – original draft, Validation, Supervision, Software, Methodology, Investigation, Data curation. **Dina Moazamian:** Writing – review & editing, Writing – original draft, Methodology, Investigation, Data curation, Validation. **Hamidreza Shaterian Mohammadi:** Writing – review & editing, Writing – original draft, Methodology, Investigation, Data curation. **Yajun Ma:** Writing – review & editing, Conceptualization, Investigation, Methodology, Data curation. **Hyungseok Jang:** Writing – review & editing, Investigation. **Behnam Namiranian:** Writing – review & editing, Investigation, Validation. **Soo Hyun Shin:** Writing – review & editing, Investigation. **Salem Alenezi:** Writing – review & editing, Investigation. **Sameer B. Shah:** Writing – review & editing, Investigation, Methodology, Resources. **Christine B. Chung:** Writing – review & editing, Conceptualization, Methodology, Investigation, Resources. **Eric Y. Chang:** Writing – review & editing, Conceptualization, Investigation, Methodology, Resources. **Jiang Du:** Writing – original draft, Writing – review & editing, Conceptualization, Investigation, Resources, Methodology, Supervision.

Declaration of competing interest

The authors have no conflicts of interest to declare.

Data availability

Data will be made available on request.

Acknowledgements

The authors acknowledge grant support from the National Institutes of Health (R01AR068987, R01AR062581, R01AR075825, K01AR080257, R01AR079484, R01AR078877, and 5P30AR073761), Veterans Affairs Clinical Science and Rehabilitation R&D (I01CX001388, I01BX005952, I01CX000625, and I01CX002118), Department of Defense (W81XWH-20-1-0927), and GE Healthcare.

Appendix A. Supplementary data

Supplementary data to this article can be found online at https://doi.org/10.1016/j.bone.2024.117096.

References

[1] J. Zanker, G. Duque, Osteoporosis in older persons: old and new players, J. Am. Geriatr. Soc. 67 (2019) 831–840, https://doi.org/10.1111/jgs.15716.
[2] S. Guerri, D. Mercatelli, M.P.A. Gómez, A. Napoli, G. Battista, G. Guglielmi, A. Bazzocchi, Quantitative imaging techniques for the assessment of osteoporosis and sarcopenia, Quant Imaging Med Surg 8 (2018) 60–85, https://doi.org/10.21037/qims.2018.01.05.
[3] A.C. Looker, S.M. Frenk, Percentage of Adults Aged 65 and Over With Osteoporosis or Low Bone Mass at the Femur Neck or Lumbar Spine: United States, 2005–2010, Centers for Disease Control and Prevention, 2015, pp. 2005–2010.
[4] J.A. Kanis, O. Johnell, A. Oden, H. Johansson, E. McCloskey, FRAXTM and the assessment of fracture probability in men and women from the UK, Osteoporos. Int. 19 (2008) 385–397, https://doi.org/10.1007/s00198-007-0543-5.
[5] Y.N. Yeni, C.U. Brown, T.L. Norman, Influence of bone composition and apparent density on fracture toughness of the human femur and tibia, Bone (1998), https://doi.org/10.1016/S8756-3282(97)00227-5.
[6] C.E.D.H. De Laet, B.A. Van Hout, H. Burger, A. Hofman, H.A.P. Pols, Bone density and risk of hip fracture in men and women: cross sectional analysis, Br. Med. J. 315 (1997) 11–15, https://doi.org/10.1136/bmj.315.7102.221.
[7] K. Trajanoska, J.D. Schoufour, E.A.L. de Jonge, B.C.T. Kieboom, M. Mulder, B. H. Stricker, T. Voortman, A.G. Uitterlinden, E.H.G. Oei, M. Arfan Ikram, M. Carola Zillikens, F. Rivadeneira, L. Oei, Fracture incidence and secular trends between 1989 and 2013 in a population based cohort: the Rotterdam Study, Bone 114 (2018) 116–124, https://doi.org/10.1016/j.bone.2018.06.004.
[8] S.R. Cummings, Are patients with hip fractures more osteoporotic? Review of evidence, American Journal of Medicine 8 (1985) 487–494.
[9] D. Marshall, O. Johnell, H. Wedel, Meta-analysis of how well measures of bone mineral density predict occurrence of osteoporotic fractures, Br. Med. J. 18 (1996) 1254–1259, https://doi.org/10.1136/bmj.312.7041.1254.
[10] J.A. Kanis, O. Johnell, A. Oden, A. Dawson, C. De Laet, B. Jonsson, Ten year probabilities of osteoporotic fractures according to BMD and diagnostic thresholds, Osteoporos. Int. (2001), https://doi.org/10.1007/s001980170006.
[11] C.R. Russo, F. Lauretani, S. Bandinelli, B. Bartali, A. Di Iorio, S. Volpato, J. M. Guralnik, T. Harris, L. Ferrucci, Aging bone in men and women: beyond changes in bone mineral density, Osteoporos. Int. (2003), https://doi.org/10.1007/s00198-002-1322-y.
[12] S.C.E. Schuit, M. Van Der Klift, A.E.A.M. Weel, C.E.D.H. De Laet, H. Burger, E. Seeman, A. Hofman, A.G. Uitterlinden, J.P.T.M. Van Leeuwen, H.A.P. Pols, Fracture incidence and association with bone mineral density in elderly men and women: the Rotterdam Study, Bone 34 (2004) 195–202, https://doi.org/10.1016/j.bone.2003.10.001.
[13] B. Van Rietbergen, S. Majumdar, W. Pistoia, D.C. Newitt, M. Kothari, A. Laib, P. Ruegsegger, Assessment of cancellous bone mechanical properties from micro-FE models based on micro-CT, pQCT and MR images, Technol. Health Care 6 (1998) 413–420, https://doi.org/10.3233/thc-1998-65-613.
[14] D.C. Newitt, S. Majumdar, B. Van Rietbergen, G. Von Ingersleben, S.T. Harris, H. K. Genant, C. Chesnut, P. Garnero, B. MacDonald, In vivo assessment of architecture and micro-finite element analysis derived indices of mechanical properties of trabecular bone in the radius, Osteoporos. Int. 13 (2002) 6–17, https://doi.org/10.1007/s198-002-8332-0.
[15] D.C. Newitt, B. Van Rietbergen, S. Majumdar, Processing and analysis of in vivo high-resolution MR images of trabecular bone for longitudinal studies: reproducibility of structural measures and micro-finite element analysis derived mechanical properties, Osteoporos. Int. 13 (2002) 278–287, https://doi.org/10.1007/s001980200027.
[16] B. Van Rietbergen, S. Majumdar, D. Newitt, B. MacDonald, High-resolution MRI and micro-FE for the evaluation of changes in bone mechanical properties during longitudinal clinical trials: application to calcaneal bone in postmenopausal women after one year of idoxifene treatment, Clin. Biomech. 17 (2002) 81–88, https://doi.org/10.1016/S0268-0033(01)00110-3.
[17] C.S. Rajapakse, J. Magland, H. Zhang, X.S. Liu, S.L. Wehrli, X.E. Guo, F.W. Wehrli, Implications of noise and resolution on mechanical properties of trabecular bone estimated by image-based finite-element analysis, J. Orthop. Res. 27 (2009) 1263–1271, https://doi.org/10.1002/jor.20877.
[18] N. Zhang, J.F. Magland, C.S. Rajapakse, Y.A. Bhagat, F.W. Wehrli, Potential of in vivo MRI-based nonlinear finite-element analysis for the assessment of trabecular bone post-yield properties, Med. Phys. 40 (2013) 1–10, https://doi.org/10.1118/1.4802085.
[19] N. Zhang, J.F. Magland, C.S. Rajapakse, S.C.B. Lam, F.W. Wehrli, Assessment of trabecular bone yield and post-yield behavior from high-resolution MRI-based nonlinear finite element analysis at the distal radius of premenopausal and postmenopausal women susceptible to osteoporosis, Acad. Radiol. 20 (2013) 1584–1591, https://doi.org/10.1016/j.acra.2013.09.005.
[20] J.S. Bauer, R. Monetti, R. Krug, M. Matsuura, D. Mueller, F. Eckstein, E. J. Rummeny, E.M. Lochmueller, C.W. Raeth, T.M. Link, Advances of 3T MR imaging in visualizing trabecular bone structure of the calcaneus are partially SNR-independent: analysis using simulated noise in relation to micro-CT, 1.5T MRI, and biomechanical strength, J. Magn. Reson. Imaging (2009), https://doi.org/10.1002/jmri.21625.
[21] V. Vieth, T.M. Link, A. Lotter, T. Persigehl, D. Newitt, W. Heindel, S. Majumdar, Does the trabecular bone structure depicted by high-resolution MRI of the calcaneus reflect the true bone structure? Investig. Radiol. (2001) https://doi.org/10.1097/00004424-200104000-00003.
[22] J.F. Magland, M.J. Wald, F.W. Wehrli, Spin-echo micro-MRI of trabecular bone using improved 3D fast large-angle spin-echo (FLASE), Magn. Reson. Med. 61 (2009) 1114–1121, https://doi.org/10.1002/mrm.21905.
[23] S. Jerban, S. Alenezi, A.M. Afsahi, Y. Ma, J. Du, C.B. Chung, E.Y. Chang, MRI-based mechanical competence assessment of bone using micro finite element analysis (micro-FEA): review, Magn. Reson. Imaging 88 (2022) 9–19, https://doi.org/10.1016/j.mri.2022.01.009.
[24] X. Li, D. Kuo, A.L. Schafer, A. Porzig, T.M. Link, D. Black, A.V. Schwartz, Quantification of vertebral bone marrow fat content using 3 Tesla MR spectroscopy: reproducibility, vertebral variation, and applications in osteoporosis, J. Magn. Reson. Imaging 33 (2011) 974–979, https://doi.org/10.1002/jmri.22489.
[25] S. Mostoufi-Moab, J. Magland, E.J. Isaacoff, W. Sun, C.S. Rajapakse, B. Zemel, F. Wehrli, K. Shekdar, J. Baker, J. Long, M.B. Leonard, Adverse fat depots and marrow adiposity are associated with skeletal deficits and insulin resistance in long-term survivors of pediatric hematopoietic stem cell transplantation, J. Bone Miner. Res. 30 (2015) 1657–1666, https://doi.org/10.1002/jbmr.2512.
[26] S. Jerban, Y. Ma, B. Namiranian, A. Ashir, H. Shirazian, W. Zhao, M. Wu, Z. Cai, N. Le, J. Du, E.Y. Chang, Age-related decrease in collagen proton fraction in tibial tendons estimated by magnetization transfer modeling of ultrashort echo time magnetic resonance imaging (UTE-MRI), Sci Rep November (2019) 17974, https://doi.org/10.1038/s41598-019-54559-3.
[27] Y. Ma, H. Jang, S. Jerban, E.Y. Chang, C.B. Chung, G.M. Bydder, J. Du, Making the invisible visible—ultrashort echo time magnetic resonance imaging: technical developments and applications, Appl. Phys. Rev. 9 (2022) 041303, https://doi.org/10.1063/5.0086459.
[28] F.W. Wehrli, H.K. Song, P.K. Saha, A.C. Wright, Quantitative MRI for the assessment of bone structure and function, NMR Biomed. 19 (2006) 731–764, https://doi.org/10.1002/nbm.

[29] X.H. Zhang, X.S. Liu, B. Vasilic, F.W. Wehrli, M. Benito, C.S. Rajapakse, P. J. Snyder, X.E. Guo, In vivo μMRI-based finite element and morphological analyses of tibial trabecular bone in eugonadal and hypogonadal men before and after testosterone treatment, J. Bone Miner. Res. 23 (2008) 1426–1434, https://doi.org/10.1359/jbmr.080405.
[30] F.W. Wehrli, C.S. Rajapakse, J.F. Magland, P.J. Snyder, Mechanical implications of estrogen supplementation in early postmenopausal women, J. Bone Miner. Res. 25 (2010) 1406–1414, https://doi.org/10.1002/jbmr.33.
[31] C.S. Rajapakse, M.B. Leonard, Y.A. Bhagat, W. Sun, J.F. Magland, F.W. Wehrli, Micro-MR imaging-based computational biomechanics demonstrates reduction in cortical and trabecular bone strength after renal transplantation, Radiology 262 (2012) 912–920, https://doi.org/10.1148/radiol.11111044.
[32] C.S. Rajapakse, E.A. Kobe, A.S. Batzdorf, M.W. Hast, F.W. Wehrli, Accuracy of MRI-based finite element assessment of distal tibia compared to mechanical testing, Bone 108 (2018) 71–78, https://doi.org/10.1016/j.bone.2017.12.023.
[33] S. Majumdar, Magnetic resonance imaging of trabecular bone structure, Top. Magn. Reson. Imaging 13 (2002) 323–334, https://doi.org/10.1097/00002142-200210000-00004.
[34] A.K. Sharma, N.D. Toussaint, G.J. Elder, R. Masterson, S.G. Holt, P.L. Robertson, P. R. Ebeling, P. Baldock, R.C. Miller, C.S. Rajapakse, A.L. Hong, M. Ispiryan, M. V. Padalkar, B.C. Jones, A.S. Batzdorf, S.S. Shetye, N. Pleshko, C.S. Rajapakse, A. K. Sharma, N.D. Toussaint, G.J. Elder, R. Masterson, S.G. Holt, P.L. Robertson, P. R. Ebeling, P. Baldock, R.C. Miller, C.S. Rajapakse, F.W. Ehrli, S. Majumdar, Magnetic resonance imaging based assessment of bone microstructure as a non-invasive alternative to histomorphometry in patients with chronic kidney disease, Bone 114 (2018) 14–21, https://doi.org/10.1016/j.bone.2018.05.029.
[35] G. Chang, C.M. Deniz, S. Honig, C.S. Rajapakse, K. Egol, R.R. Regatte, R. Brown, Feasibility of three-dimensional MRI of proximal femur microarchitecture at 3 tesla using 26 receive elements without and with parallel imaging, J. Magn. Reson. Imaging 40 (2014) 229–238, https://doi.org/10.1002/jmri.24345.
[36] M. Han, K. Chiba, S. Banerjee, J. Carballido-Gamio, R. Krug, Variable flip angle three-dimensional fast spin-echo sequence combined with outer volume suppression for imaging trabecular bone structure of the proximal femur, J. Magn. Reson. Imaging 41 (2015) 1300–1310, https://doi.org/10.1002/jmri.24673.
[37] F.W. Wehrli, Structural and functional assessment of trabecular and cortical bone by micro magnetic resonance imaging, J. Magn. Reson. Imaging 25 (2007) 390–409, https://doi.org/10.1002/jmri.20807.
[38] S. Majumdar, D. Thomasson, A. Shimakawa, H.K. Genant, Quantitation of the susceptibility difference between trabecular bone and bone marrow: experimental studies, Magn. Reson. Med. 22 (1991) 111–127, https://doi.org/10.1002/mrm.1910220112.
[39] J.M. Patsch, X. Li, T. Baum, S.P. Yap, D.C. Karampinos, A.V. Schwartz, T.M. Link, Bone marrow fat composition as a novel imaging biomarker in postmenopausal women with prevalent fragility fractures, J. Bone Miner. Res. 28 (2013) 1721–1728, https://doi.org/10.1002/jbmr.1950.
[40] R.O. Ritchie, M.J. Buehler, P. Hansma, Plasticity and toughness in bone, Phys. Today 62 (2009) 41–47, https://doi.org/10.1063/1.3156332.
[41] S. Jerban, H. Jang, E.Y. Chang, S. Bukata, J. Du, C.B. Chung, Bone biomarkers based on magnetic resonance imaging, Semin. Musculoskelet. Radiol. 28 (2024) 062–077, https://doi.org/10.1055/s-0043-1776431.
[42] S. Jerban, Y. Ma, E.Y. Chang, C.B. Chung, G.M. Bydder, J. Du, A UTE-based biomarker panel in osteoporosis, in: MRI of Short and Ultrashort-T_2 Tissues, Springer International Publishing, Cham, 2023, pp. 427–439, https://doi.org/10.1007/978-3-031-35197-6_34.
[43] T. Speidel, C.H. Meyer, V. Rasche, Non-cartesian Imaging, 2022, pp. 481–498, https://doi.org/10.1016/B978-0-12-824460-9.00028-5.
[44] M. Bydder, M. Carl, G.M. Bydder, J. Du, MRI chemical shift artifact produced by center-out radial sampling of k-space: a potential pitfall in clinical diagnosis, Quant Imaging Med Surg 11 (2021) 3677–3683, https://doi.org/10.21037/qims-21-115.
[45] P.K. Saha, F.W. Wehrli, Measurement of trabecular bone thickness in the limited resolution regime of in vivo MRI by fuzzy distance transform, IEEE Trans. Med. Imaging 23 (2004) 53–62, https://doi.org/10.1109/TMI.2003.819925.
[46] S. Majumdar, H.K. Genant, S. Grampp, D.C. Newitt, V.H. Truong, J.C. Lin, A. Mathur, Correlation of trabecular bone structure with age, bone mineral density, and osteoporotic status: In vivo studies in the distal radius using high resolution magnetic resonance imaging, J. Bone Miner. Res. 12 (1) (1997 Jan) 111–118, https://doi.org/10.1359/jbmr.1997.12.1.111. PMID: 9240733.
[47] J. Carballido-Gamio, C. Phan, T.M. Link, S. Majumdar, Characterization of trabecular bone structure from high-resolution magnetic resonance images using fuzzy logic, Magn. Reson. Imaging 24 (2006) 1023–1029, https://doi.org/10.1016/j.mri.2006.04.010.
[48] O. Beuf, D.C. Newitt, L. Mosekilde, S. Majumdar, Trabecular structure assessment in lumbar vertebrae specimens using quantitative magnetic resonance imaging and relationship with mechanical competence, J. Bone Miner. Res. 16 (2001) 1511–1519, https://doi.org/10.1359/jbmr.2001.16.8.1511.
[49] J.A. MacNeil, S.K. Boyd, Accuracy of high-resolution peripheral quantitative computed tomography for measurement of bone quality, Med. Eng. Phys. 29 (2007) 1096–1105, https://doi.org/10.1016/j.medengphy.2006.11.002.
[50] P.A. Hulme, S.K. Boyd, S.J. Ferguson, Regional variation in vertebral bone morphology and its contribution to vertebral fracture strength, Bone 41 (2007) 946–957, https://doi.org/10.1016/j.bone.2007.08.019.
[51] J.A. MacNeil, M.R. Doschak, R.F. Zernicke, S.K. Boyd, Preservation of periarticular cancellous morphology and mechanical stiffness in post-traumatic experimental osteoarthritis by antiresorptive therapy, Clin. Biomech. 23 (2008) 365–371, https://doi.org/10.1016/j.clinbiomech.2007.10.015.
[52] H.M. MacDonald, K.K. Nishiyama, J. Kang, D.A. Hanley, S.K. Boyd, Age-related patterns of trabecular and cortical bone loss differ between sexes and skeletal sites: a population-based HR-pQCT study, J. Bone Miner. Res. 26 (2011) 50–62, https://doi.org/10.1002/jbmr.171.
[53] M.L. Bouxsein, S.K. Boyd, B.A. Christiansen, R.E. Guldberg, K.J. Jepsen, R. Müller, Guidelines for assessment of bone microstructure in rodents using micro-computed tomography, J. Bone Miner. Res. 25 (2010) 1468–1486, https://doi.org/10.1002/jbmr.141.
[54] J.F. Griffith, D.K.W. Yeung, H.T. Ma, J.C.S. Leung, T.C.Y. Kwok, P.C. Leung, Bone marrow fat content in the elderly: a reversal of sex difference seen in younger subjects, J. Magn. Reson. Imaging 36 (2012) 225–230, https://doi.org/10.1002/jmri.23619.
[55] P. Hardouin, V. Pansini, B. Cortet, Bone marrow fat, Joint Bone Spine 81 (2014) 313–319, https://doi.org/10.1016/j.jbspin.2014.02.013.
[56] G.P. Liney, C.P. Bernard, D.J. Manton, L.W. Turnbull, C.M. Langton, Age, gender, and skeletal variation in bone marrow composition: a preliminary study at 3.0 Tesla, J. Magn. Reson. Imaging 26 (2007) 787–793, https://doi.org/10.1002/jmri.21072.
[57] R. Oftadeh, M. Perez-Viloria, J.C. Villa-Camacho, A. Vaziri, A. Nazarian, Biomechanics and mechanobiology of trabecular bone: a review, J. Biomech. Eng. 137 (2015) 1–15, https://doi.org/10.1115/1.4029176.
[58] E. Novitskaya, P.-Y. Chen, E. Hamed, L. Jun, V. Lubarda, I. Jasiuk, J. Mckittrick, Recent advances on the measurement and calculation of the elastic moduli of cortical and trabecular bone: a review, Theoretical and Applied Mechanics 38 (2011) 209–297, https://doi.org/10.2298/TAM1103209N.
[59] D. Ulrich, B. Van Rietbergen, A. Laib, P. Ruegsegger, The ability of three-dimensional structural indices to reflect mechanical aspects of trabecular bone, Bone 25 (1999) 55–60, https://doi.org/10.1016/S8756-3282(99)00098-8.
[60] H. Rosenthal, K.R. Thulborn, D.I. Rosenthal, S.H. Kim, B.R. Rosen, Magnetic susceptibility effects of trabecular bone on magnetic resonance imaging of bone marrow, Invest Radiol. 25 (2) (1990 Feb) 173–178, https://doi.org/10.1097/00004424-199002000-00013. PMID:2312252.
[61] J.C. Ford, F.W. Wehrli, In vivo quantitative characterization of trabecular bone by NMR interferometry and localized proton spectroscopy, Magn. Reson. Med. 17 (2) (1991) 543–551, https://doi.org/10.1002/mrm.1910170225.
[62] F.W. Wehrli, Magnetic resonance of calcified tissues, J. Magn. Reson. 229 (2013) 35–48, https://doi.org/10.1016/j.jmr.2012.12.011.
[63] T.M. Link, S. Majumdar, P. Augat, J.C. Lin, D. Newitt, N.E. Lane, H.K. Genant, Proximal femur: assessment for osteoporosis with T2* decay characteristics at MR imaging, Radiology 209 (1998) 531–536, https://doi.org/10.1148/radiology.209.2.9807585.
[64] Y. Chen, Y. Guo, Y. Feng, X. Zhang, Y. Mei, X. Zhang, Bone susceptibility mapping with MRI is an alternative and reliable biomarker of osteoporosis in postmenopausal women, Eur. Radiol. 28 (2018) 5027–5034, https://doi.org/10.1007/s00330-018-5419-x.
[65] J. Diefenbach, Maximilian N. Meineke, S. Ruschke, T. Baum, A. Gersing, D. C. Karampinos, On the sensitivity of quantitative susceptibility mapping for measuring trabecular bone density, Magn. Reson. Med. 81 (2018) 1739–1754, https://doi.org/10.1002/mrm.27531.
[66] Y. Wu, G. Dai, J.L. Ackerman, M.I. Hrovat, M.J. Glimcher, B.D. Snyder, A. Nazarian, D.A. Chesler, Water- and fat-suppressed proton projection MRI (WASPI) of rat femur bone, Magn. Reson. Med. 57 (2007) 554–567, https://doi.org/10.1002/mrm.21174.
[67] M. Weiger, M. Stampanoni, K.P. Pruessmann, Direct depiction of bone microstructure using MRI with zero echo time, Bone 54 (2013) 44–47, https://doi.org/10.1016/j.bone.2013.01.027.
[68] M.C. Wurnig, M. Calcagni, D. Kenkel, M. Vich, M. Weiger, G. Andreisek, F. W. Wehrli, A. Boss, Characterization of trabecular bone density with ultra-short echo-time MRI at 1.5, 3.0 and 7.0 T - comparison with micro-computed tomography, NMR Biomed. 27 (2014) 1159–1166, https://doi.org/10.1002/nbm.3169.
[69] Y.J. Ma, Y. Chen, L. Li, Z. Cai, Z. Wei, S. Jerban, H. Jang, E.Y. Chang, J. Du, Trabecular bone imaging using a 3D adiabatic inversion recovery prepared ultrashort TE Cones sequence at 3T, Magn. Reson. Med. 83 (2020) 1640–1651, https://doi.org/10.1002/mrm.28027.
[70] S. Majumdar, H.K. Genant, A review of the recent advances in magnetic resonance imaging in the assessment of osteoporosis, Osteoporos. Int. 5 (1995) 79–92, https://doi.org/10.1007/BF01623308.
[71] J. Du, G.M. Bydder, Qualitative and quantitative ultrashort-TE MRI of cortical bone, NMR Biomed. 26 (2013) 489–506, https://doi.org/10.1002/nbm.2906.